J. Fluid Mech. (2022), *vol*. 953, A3, doi:10.1017/jfm.2022.941

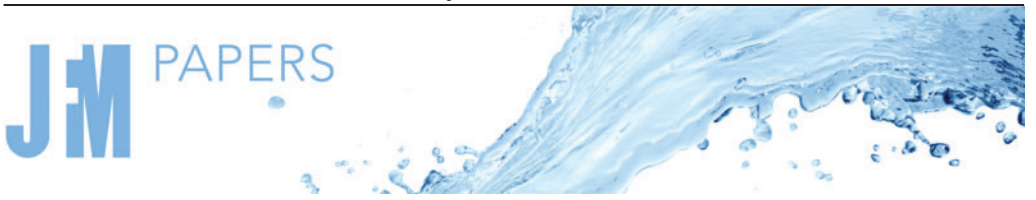

On the turbulence modelling of waves breaking on a vertical pile

Yuzhu Li[1,2,†] **and David R. Fuhrman**[2]

[1]Department of Civil and Environmental Engineering, National University of Singapore, 117576, Republic of Singapore

[2]Department of Mechanical Engineering, Section for Fluid Mechanics, Coastal and Maritime Engineering, Technical University of Denmark, 2800 Kgs. Lyngby, Denmark

(Received 22 March 2022; revised 15 August 2022; accepted 4 November 2022)

Incipient wave breaking on a vertical circular pile is simulated with a Reynolds stress–ω turbulence model. Comparison of results simulated with a stabilized two-equation turbulence model, as well as no turbulence model, demonstrates that the breaking point and the peak force on a vertical cylinder due to incipient breaking should not be affected by the turbulence closure model, provided that it is stable and the simulations are converged. Notably, the present results show that the build-up to peak force induced by incipient wave breaking can be accurately predicted without any turbulence closure model. However, for the prediction of the secondary load cycle (SLC), proper turbulence modelling is required, as this process involves both turbulence production and lee-side flow separation. The Reynolds stress–ω model is demonstrated to predict the SLC more accurately than a stabilized two-equation k–ω turbulence model, as the flow separation points and vorticity field are better predicted. Some existing studies indicate that the generation of the SLC does not necessarily result from flow separation, but is rather due to the suction force. The present work finds that the occurrence and point of flow separation significantly affect the magnitude of the suction force, which hence affects the SLC prediction significantly. For waves breaking on a vertical pile, proper turbulence modelling is therefore essential for accurate SLC predictions. (In the above, k is the turbulent kinetic energy density and ω is the specific dissipation rate.)

Key words: turbulence modelling, wave breaking, wave–structure interactions

1. Introduction

Breaking waves can have severe impacts on coastal structures such as wind turbine foundations, seawalls, breakwaters and bottom-fixed oscillating water column wave

† Email address for correspondence: pearl.li@nus.edu.sg

energy converters. As waves propagate on sloped seabeds towards the shoreline, they undergo shoaling where the wave length decreases and the wave height increases. At a certain depth (depending on the wave characteristics and the slope of the beach), the crest velocity will exceed the celerity of wave propagation and the waves will become unstable and break. Once wave breaking occurs, a large amount of wave energy will dissipate in the form of turbulence. The load exerted on coastal structures by breaking waves differs from non-breaking waves in that it is superposed with an additional, strong and transient force over a short time (Irschik, Sparboom & Oumeraci 2004). The commonly used Morison equation (Morison, Johnson & Schaaf 1950) for determining non-breaking wave forces acting on a structure can therefore underpredict such breaking wave-induced forces. Thereby, an extra empirical term is usually needed if breaking-induced forces are calculated with the Morison equation (Wienke & Oumeraci 2005).

The extensive use of vertical piles as basic components of coastal structures, e.g. monopile wind turbine foundations and pile-supported jetties, has made the study of wave impact on piles in the breaking zone of major practical importance. To investigate the breaking wave forces on a vertical pile located on a sloped bed, many earlier studies have adopted experimental approaches since no theory was available for predicting such breaking wave force (Apelt & Piorewicz 1987). Since the 1950s, experimental studies have been conducted with focus on the peak force induced by breaking waves on a vertical pile and the controlling factors to the maximum force. For example, Hall (1958) measured the maximum breaking wave forces on a vertical pile located on a beach slope of 1 : 10. He noticed that the maximum force is very sensitive to the position of the pile with respect to the breaking point. Honda & Mitsuyasu (1974) later conducted a similar experiment on a 1 : 15 sloping beach. Their measured wave forces were compared with the analytical values from the Morison equation, and it was found that the measured maximum wave forces were approximately five times larger. They also compared their measurements with those from Hall (1958) and analysed the effect of the bed slope on the peak force. Apelt & Piorewicz (1987) conducted similar experiments on a 1 : 15 sloping beach. They found that the maximum breaking wave force on a vertical pile is not only influenced by the bottom slope and wave steepness, but also by the cylinder diameter to wave height ratio. Based on experimental data, Wiegel (1982) proposed an empirical approach to predict forces exerted by breaking waves, which requires the magnitude of a curling factor, though its accuracy has not yet been fully proved. Kyte & Tørum (1996) conducted experimental studies on plunging breaking wave forces on a vertical pile both in regular and irregular wave conditions. They have also measured the duration of the resulting impact forces and proposed engineering formulae to estimate the wave forces. A recent experiment conducted by Irschik *et al.* (2004) measured the breaking wave forces on a slender pile located at the end of a 1 : 10 sloping beach. Their experiments are seemingly the most often modelled in recent computational fluid dynamics (CFD) studies involving progressive waves breaking on a vertical pile, e.g. Choi, Lee & Gudmestad (2015), Jose *et al.* (2017), Kamath *et al.* (2016), Bihs *et al.* (2016), Liu *et al.* (2019) and Qu, Liu & Ong (2021). The experimental data of Irschik *et al.* (2004) have been analysed and for the first time been presented in the work of Choi *et al.* (2015), where the effect of dynamic amplification due to the structural vibration was filtered such that the net breaking wave force could be used to validate CFD models utilizing a fixed structure.

In most recent CFD studies involving breaking waves on a vertical pile, Reynolds-averaged Navier–Stokes (RANS) equations based turbulence models have been used as closure, e.g. Jose *et al.* (2017), Bihs *et al.* (2016), Liu *et al.* (2019), Qu *et al.* (2021) and Ghadirian & Bredmose (2020). For such a three-dimensional (3-D) CFD problem involving two-phase fluids (water and air) interacting with a structure, direct numerical

simulation (DNS) is unrealistic due to its large computational costs. Large eddy simulation (LES) is less expensive than DNS, but still requires much higher computational cost than RANS models (see, e.g. § 9.6 of Sumer & Fuhrman 2020). The numerical study of Choi *et al.* (2015) used LES with a Smagorinsky (1963) sub-grid scale model based on the finite difference method (FDM). Free surface tracking was based on the volume-of-fluid (VOF) method. Jose *et al.* (2017) compared the FDM-based LES model used in Choi *et al.* (2015) to the finite volume method based RANS two-equation model, i.e. the standard k–ω shear stress transport (SST) model (Menter 1994) (where k is the turbulent kinetic energy density and ω is the specific dissipation rate). They concluded that the results are more or less the same: both models reasonably predicted the peak force, but yielded a delayed prediction of the secondary load cycle (SLC), while the model used in Choi *et al.* (2015) required a much larger number of cells and computational cost. Kamath *et al.* (2016) and Bihs *et al.* (2016) modelled the experiment conducted by Irschik *et al.* (2004) using the standard k–ω model as turbulence closure. They incorporated an empirical relationship for the specific turbulence dissipation at the free surface region (Naot & Rodi 1982). This modification is similar to the buoyancy-modified k–ω model proposed in Devolder, Troch & Rauwoens (2018) that aimed to remove the turbulence pollution from the air phase to the water phase. Kamath *et al.* (2016) calculated wave forces on the vertical cylinder with waves breaking before, on and behind the cylinder. It was shown that when the overturning wave crest hits the cylinder just below the wave crest level, the force will be the largest among these scenarios. Liu *et al.* (2019) modelled the Irschik *et al.* (2004) experiment using the standard k–ω SST turbulence closure model, though their cylinder was located half a diameter downstream relative to that in, for example, Choi *et al.* (2015), Kamath *et al.* (2016), Bihs *et al.* (2016) and Qu *et al.* (2021).

Recently, Qu *et al.* (2021) evaluated different RANS-based two-equation turbulence models for simulating the experiment of Irschik *et al.* (2004), in which waves are again breaking on a vertical cylinder with its centre located at the end of the 1 : 10 slope. They compared the numerical CFD results using (*a*) no turbulence model (assuming laminar flow), (*b*) the standard k–ω SST model (Menter 1994) with and without a buoyancy production term, (*c*) the stabilized k–ω SST model (Larsen & Fuhrman 2018) with and without a buoyancy production term, and (*d*) the standard realizable k–ε model (Shih *et al.* 1995) (where ε is the turbulence dissipation rate). First, it was shown that both the standard k–ω SST model and the standard realizable k–ε model predicted large turbulence kinetic energy k in the potential flow region before wave breaking (which is very likely unphysical). This is consistent with the analysis in the recent studies of Larsen & Fuhrman (2018) and Fuhrman & Li (2020). They proved that these (in fact, seemingly all) two-equation models in their standard forms are unstable in the potential flow region beneath surface waves, which can lead to unphysical turbulence over-production (exponential growth) in the pre-breaking zones. This may artificially decay the waves and, hence, lead to delayed breaking. Moreover, as shown by Fuhrman & Li (2020), the standard realizable k–ε model can have an exponential growth rate of turbulence that is three times larger than other models when the initial conditions fall into the unstable zone (as shown by Fuhrman & Li (2020), this model is conditionally unstable, in contrast to other standard two-equation models analysed thus far that are unconditionally unstable). The realizable k–ε model may hence be extremely unstable for simulating progressive waves. The results in Qu *et al.* (2021) are generally consistent with this analysis, in that the standard realizable k–ε model resulted in the highest pre-breaking turbulence levels, and with the breaking point delayed to behind the cylinder, in contrast to their other models. To eliminate turbulence over-production prior to the breaking region, Larsen &

Fuhrman (2018) and Fuhrman & Li (2020) formally stabilized such two-equation turbulence models with a simple reformulation of the eddy viscosity. Consistent with these expectations, Qu *et al.* (2021) also showed that the stabilized k–ω SST model of Larsen & Fuhrman (2018) does not produce unphysical turbulence in the pre-breaking region. It is worthwhile to mention that the buoyancy production term should also seemingly be incorporated in turbulence models when simulating breaking waves (Devolder *et al.* 2018; Larsen & Fuhrman 2018; Fuhrman & Li 2020) to avoid potential turbulence pollution from the air phase to the water phase. It is emphasized that while the buoyancy production term combats this problem, it does nothing to prevent turbulence over-production in the bulk potential flow region; see the discussion of Fuhrman & Larsen (2020). Although Larsen & Fuhrman (2018) and Fuhrman & Li (2020) have demonstrated that stabilized two-equation turbulence models can accurately predict the breaking point, the results of Qu *et al.* (2021) suggest that the stabilized k–ω SST model fails to predict the breaking point accurately. Their results likewise suggest that the breaking location is influenced by the choice of turbulence model, a point that will be thoroughly addressed in the present work. Moreover, none of the turbulence models employed by Qu *et al.* (2021) were able to provide consistent accuracy in terms of the free surface elevation, the breaking point, the induced breaking wave force and the turbulence characteristics. Their findings could possibly be due to the large Courant number ($Co = \bar{u}_i \Delta t / \Delta x_i$, where $\bar{u}_i$ is the mean flow velocity, Δt and Δx_i are the time and grid length intervals, respectively) used in their simulations (with $Co = 0.5$), which will also be specifically investigated in the present work. It is noted that Larsen, Fuhrman & Roenby (2019) performed a detailed study on CFD modelling of non-breaking progressive waves using the VOF method in OpenFOAM. It was shown that a sufficiently small Courant number is required ($Co \leq 0.1$) to ensure good numerical accuracy in both free surface elevations and velocity kinematics, indicating that many previous simulations have likely not been converged.

Besides the peak force that has been extensively investigated in prior experimental and numerical studies, the SLC, which is sometimes linked to 'ringing', i.e. vibrations that appear at natural frequencies of the structures (Chaplin, Rainey & Yemm 1997; Grue & Huseby 2002), has also been a focus in several recent studies, e.g. Kristiansen & Faltinsen (2017), Ghadirian & Bredmose (2020), Antolloni *et al.* (2020) and Xu & Wang (2021). The SLC (first reported by Grue, Bjørshol & Strand 1993) is a high-order nonlinear wave force that occurs at a frequency above the third harmonic (Antolloni *et al.* 2020). It can be close to the natural frequency of coastal or offshore structures, hence, causing so-called 'ringing' that contributes to structural fatigue. To date, the physical cause driving the SLC is still debated. Several explanations have been made in previous studies. For example, recent numerical simulations by Paulsen *et al.* (2014) and Kristiansen & Faltinsen (2017) have investigated the role of vortex generation on the SLC. Simulations of Paulsen *et al.* (2014) showed that the occurrence of the SLC is related to the downstream vortex formation. Kristiansen & Faltinsen (2017) conducted both an experimental study and a two-dimensional (2-D) cross-flow CFD simulation on the higher harmonic wave loads on a vertical pile. They suggested that the local rear run-up, which is caused by the pressure due to flow separation, is responsible for the SLC. This is in contrast to the earlier study of Grue *et al.* (1993), who reported no flow separation while observing the SLC. A recent study of Antolloni *et al.* (2020) examined the connection between vortex generation and the SLC. They found that the vortex formation has a significant contribution to the SLC when the vertical pile is exposed to long waves. However, in short waves where no lee-side vortex is formed, SLC still persists. They concluded that the SLC may be mainly driven by gravity wave effects rather than vortex formation.

Inspired by recent CFD studies, the present work will perform novel investigations involving advanced turbulence modelling of waves breaking incipiently on a vertical pile. We will adopt a Reynolds stress model, namely the Wilcox (2006) stress–ω model, as our primary turbulence closure model. The stress–ω model breaks free from the Boussinesq approximation that is the foundation of two-equation models, and instead solves for the six components of the Reynolds stress tensor directly. The stress–ω model is chosen because it has been analysed in the recent work of Li, Larsen & Fuhrman (2022) and proven to be neutrally stable in the potential flow region beneath surface waves, thus, it naturally avoids any unphysical turbulence over-production in the pre-breaking zone. It has also shown very good accuracy in predicting surf zone breaking waves in Li *et al.* (2022) and deep-water breaking waves in Li & Fuhrman (2021). Additionally, the standard Wilcox (2006) k–ω model and the stabilized variant of Larsen & Fuhrman (2018, hereafter called the LF18 k–ω model), will also be applied for comparison. For completeness, we will likewise compare with simulations utilizing no turbulence model.

The remainder of the present paper is organized as follows: § 2 presents the turbulence closure models utilized in the present study; § 3 provides the details of the numerical set-up and boundary conditions of the simulations; § 4 demonstrates the influences of turbulence closure models and the Courant number on the predicted wave breaking point; § 5 investigates and discusses the predicted breaking wave forces in terms of the peak force and the SLC in a detailed manner; and § 6 provides the conclusions.

2. Turbulence closure models

The present simulations involving breaking waves and their interaction with a vertical pile are based on unsteady RANS equations, coupled with various turbulence closure models. In what follows we present governing equations for the various turbulence closure models utilized in the present work.

2.1. *The Wilcox (2006) k–ω model*

The widely used two-equation Wilcox (2006) k–ω turbulence model in its standard form with a buoyancy production term are expressed as

$$\frac{\partial \bar{\rho} k}{\partial t} + \bar{u}_j \frac{\partial \bar{\rho} k}{\partial x_j} = \bar{\rho} P_k - \bar{\rho} P_b - \bar{\rho} \beta^* k \omega + \frac{\partial}{\partial x_j}\left[\left(\mu + \bar{\rho}\sigma^* \frac{k}{\omega}\right)\frac{\partial k}{\partial x_j}\right], \tag{2.1}$$

$$\frac{\partial \bar{\rho} \omega}{\partial t} + \bar{u}_j \frac{\partial \bar{\rho} \omega}{\partial x_j} = -\bar{\rho} P_\omega - \bar{\rho} \beta \omega^2 + \bar{\rho}\frac{\sigma_d}{\omega}\frac{\partial k}{\partial x_j}\frac{\partial \omega}{\partial x_j} + \frac{\partial}{\partial x_j}\left[\left(\mu + \bar{\rho}\sigma \frac{k}{\omega}\right)\frac{\partial \omega}{\partial x_j}\right], \tag{2.2}$$

where x_j are the Cartesian coordinates, μ is the dynamic fluid viscosity, $\nu = \mu/\bar{\rho}$ is the kinematic fluid viscosity, $\bar{\rho}$ is the density of the fluid and t is the time. The specific Reynolds stress tensor is defined as

$$\tau_{ij} = -\overline{u_i' u_j'}, \tag{2.3}$$

where the overbar denotes Reynolds (ensemble) averaging and the prime superscript denotes turbulent fluctuations. In the k–ω model this is formulated via the Boussinesq

approximation

$$\tau_{ij} = 2\nu_t S_{ij} - \frac{2}{3}k\delta_{ij}, \tag{2.4}$$

where ν_t is the eddy viscosity, δ_{ij} is the Kronecker delta and

$$S_{ij} = \frac{1}{2}\left(\frac{\partial \bar{u}_i}{\partial x_j} + \frac{\partial \bar{u}_j}{\partial x_i}\right) \tag{2.5}$$

is the mean strain rate tensor. In (2.1) the shear production term

$$P_k = \tau_{ij}\frac{\partial \bar{u}_i}{\partial x_j} \tag{2.6}$$

is formulated in the form of eddy viscosity (again via the Boussinesq approximation), i.e.

$$P_k = p_0\nu_t, \quad p_0 = 2S_{ij}S_{ij}. \tag{2.7a,b}$$

The buoyancy production term is formulated as

$$P_b = p_b\nu_t, \quad p_b = \alpha_b^* N^2, \quad N^2 = \frac{g_i}{\rho_0}\frac{\partial \bar{\rho}}{\partial x_i}, \tag{2.8a–c}$$

where $N^2 = 0.5N_{ii}$ is half the trace of the Brunt–Väisälä frequency tensor expressed as

$$N_{ij} = \frac{1}{\rho_0}\left(g_i\frac{\partial \bar{\rho}}{\partial x_j} + g_j\frac{\partial \bar{\rho}}{\partial x_i}\right), \tag{2.9}$$

where ρ_0 is the constant reference density of the fluid and g_j is the gravitational acceleration. The eddy viscosity is calculated by

$$\nu_t = \frac{k}{\tilde{\omega}}. \tag{2.10}$$

In the Wilcox (2006) k–ω model $\tilde{\omega} = \tilde{\tilde{\omega}}$, where

$$\tilde{\tilde{\omega}} = \max\left[\omega, \lambda_1\sqrt{\frac{p_0 - p_b}{\beta^*}}\right], \tag{2.11}$$

which includes a so-called stress limiter via the second argument in the max function. Note that compared with the original Wilcox (2006) stress limiter, a buoyancy production p_b is included for the two-phase (air and water) flow applications, in consistency with (2.1). Here, we have also introduced $\tilde{\tilde{\omega}}$ for later use in § 2.2. In (2.2) the production term for ω is

expressed as

$$P_\omega = \alpha \frac{\omega}{k} \frac{\tilde{\omega}}{\tilde{\tilde{\omega}}} P_k = \alpha \frac{\omega}{\tilde{\tilde{\omega}}} p_0. \tag{2.12}$$

The closure coefficients are (Wilcox 2006, 2008)

$$\begin{aligned} &\alpha = 0.52, \quad \beta^* = 0.09, \quad \beta_0 = 0.0708, \quad \beta = \beta_0 f_\beta, \\ &\sigma = 0.5, \quad \sigma^* = 0.6, \quad \sigma_{d0} = 0.125, \end{aligned} \tag{2.13}$$

$$\sigma_d = \begin{cases} 0, & \dfrac{\partial k}{\partial x_j}\dfrac{\partial \omega}{\partial x_j} \le 0, \\ \sigma_{d0}, & \dfrac{\partial k}{\partial x_j}\dfrac{\partial \omega}{\partial x_j} > 0, \end{cases} \tag{2.14}$$

$$f_\beta = \frac{1 + 85\chi_\omega}{1 + 100\chi_\omega}, \quad \chi_\omega = \left| \frac{\Omega_{ij}\Omega_{jk}\hat{S}_{ki}}{(\beta^*\omega)^3} \right|, \quad \hat{S}_{ki} = S_{ki} - \frac{1}{2}\frac{\partial \bar{u}_m}{\partial x_m}\delta_{ki}. \tag{2.15a–c}$$

In the present work, $\lambda_1 = 0.2$ and $\alpha_b^* = 1.36$, following Larsen & Fuhrman (2018).

2.2. *The stabilized Larsen & Fuhrman (2018) k–ω turbulence model*

Previous CFD works on modelling progressive waves breaking on a sloped beach using two-equation models (e.g. the Wilcox (2006) k–ω model in § 2.1) have shown a persistent problem of over-production of turbulence in the potential flow region beneath surface waves; see, e.g. Lin & Liu (1998), Hsu, Sakakiyama & Liu (2002), Brown *et al.* (2016), Derakhti *et al.* (2016), Devolder *et al.* (2018) and Qu *et al.* (2021). This over-production of turbulence has caused progressive waves to decay during long-time simulation even before reaching the breaking point. Larsen & Fuhrman (2018) have analysed several two-equation models and found that they are unconditionally unstable in the potential flow region beneath surface waves. They have then formally stabilized the two-equation models by reformulating the eddy viscosity. The stabilization approach involves a modification to $\tilde{\omega}$,

$$\tilde{\omega} = \max\left[\tilde{\tilde{\omega}}, \lambda_2 \frac{\beta}{\beta^*\alpha}\frac{p_0}{p_\Omega}\omega\right], \tag{2.16}$$

where

$$p_\Omega = 2\Omega_{ij}\Omega_{ij}, \quad \Omega_{ij} = \frac{1}{2}\left(\frac{\partial \bar{u}_i}{\partial x_j} - \frac{\partial \bar{u}_j}{\partial x_i}\right) \tag{2.17a,b}$$

and $\tilde{\tilde{\omega}}$ is as defined in (2.11). To limit the over-production of turbulence in the potential flow region, $\lambda_2 = 0.05$ was used in breaking wave simulations of Larsen & Fuhrman (2018), and is maintained in the present work. This model will be called the LF18 k–ω model in what follows. Note that with $\lambda_2 = 0$, then $\tilde{\omega} = \tilde{\tilde{\omega}}$ and this model essentially reverts back to the Wilcox (2006) k–ω model.

2.3. *The Wilcox (2006) Reynolds stress–ω model*

As found in the recent study of Li *et al.* (2022), the Boussinesq approximation used in all two-equation models is the fundamental reason for their instability in the potential flow regions beneath non-breaking surface waves. In contrast to two-equation

RANS models, Reynolds stress turbulence models (both ω and ε types), e.g. the Launder–Reece–Rodistress–ε model (Launder, Reece & Rodi 1975) or the stress–ω model (Wilcox 2006), break free from the Boussinesq approximation. They were proved by Li *et al.* (2022) to be neutrally stable for simulating non-breaking progressive wave trains, i.e. without having the problem of over-production of turbulence in the potential flow region beneath surface waves. Li *et al.* (2022) then applied the Wilcox (2006) stress–ω model for simulating breaking waves on a sloped bed and achieved excellent accuracy, especially in the undertow velocity in the complicated inner surf zone, which even the best two-equation model in Larsen & Fuhrman (2018) (the LF18 k–ω model) failed to accurately simulate. The stress–ω model consists of six equations for the Reynolds stress components,

$$\frac{\partial \bar{\rho}\tau_{ij}}{\partial t} + \bar{u}_k \frac{\partial \bar{\rho}\tau_{ij}}{\partial x_k} = -\bar{\rho}P_{ij} + \frac{2}{3}\bar{\rho}\beta^* \omega k \delta_{ij} - \bar{\rho}\Pi_{ij} + \frac{\partial}{\partial x_k}\left[\bar{\rho}\left(\nu + \sigma^* \frac{k}{\omega}\right)\frac{\partial \tau_{ij}}{\partial x_k}\right] + \bar{\rho}\alpha_b^* \frac{k}{\omega} N_{ij} \tag{2.18}$$

and one equation for the specific dissipation rate ω, as given in (2.2). The shear production term for ω is

$$P_\omega = \alpha \frac{\omega}{k} P_k = \alpha \frac{\omega}{k} \tau_{ij} \frac{\partial \bar{u}_i}{\partial x_j}. \tag{2.19}$$

The pressure–strain correlation is

$$\Pi_{ij} = \beta^* C_1 \omega \left(\tau_{ij} + \frac{2}{3}k\delta_{ij}\right) - \hat{\alpha}\left(P_{ij} - \frac{2}{3}P\delta_{ij}\right) - \hat{\beta}\left(D_{ij} - \frac{2}{3}P\delta_{ij}\right) - \hat{\gamma}k\left(S_{ij} - \frac{1}{3}S_{kk}\delta_{ij}\right), \tag{2.20}$$

where

$$P_{ij} = \tau_{im}\frac{\partial \bar{u}_j}{\partial x_m} + \tau_{jm}\frac{\partial \bar{u}_i}{\partial x_m}, \tag{2.21}$$

$$D_{ij} = \tau_{im}\frac{\partial \bar{u}_m}{\partial x_j} + \tau_{jm}\frac{\partial \bar{u}_m}{\partial x_i}, \tag{2.22}$$

$$P = \frac{1}{2}P_{kk}, \tag{2.23}$$

$$k = -\frac{1}{2}\tau_{kk}. \tag{2.24}$$

The last term in (2.18) is the buoyancy production term as derived in Li *et al.* (2022), which is proportional to N_{ij} from (2.9). The closure coefficients are (Wilcox 2006)

$$\begin{gathered} C_1 = 1.8, \quad C_2 = 10/19, \quad \hat{\alpha} = (8 + C_2)/11, \\ \hat{\beta} = (8C_2 - 2)/11, \quad \hat{\gamma} = (60C_2 - 4)/55, \quad \alpha = 0.52, \\ \beta^* = 0.09, \quad \beta_0 = 0.0708, \quad \beta = \beta_0 f_\beta, \\ \sigma = 0.5, \quad \sigma^* = 0.6, \quad \sigma_{d0} = 0.125, \end{gathered} \tag{2.25}$$

$$\sigma_d = \begin{cases} 0, & \dfrac{\partial k}{\partial x_j}\dfrac{\partial \omega}{\partial x_j} \leq 0, \\ \sigma_{d0}, & \dfrac{\partial k}{\partial x_j}\dfrac{\partial \omega}{\partial x_j} \geq 0, \end{cases} \tag{2.26}$$

$$f_\beta = \frac{1 + 85\chi_\omega}{1 + 100\chi_\omega}, \quad \chi_\omega = \left| \frac{\Omega_{ij}\Omega_{jk}\hat{S}_{ki}}{(\beta^*\omega)^3} \right|, \quad \hat{S}_{ki} = S_{ki} - \frac{1}{2}\frac{\partial \bar{u}_m}{\partial x_m}\delta_{ki} \tag{2.27a,b}$$

and $\alpha_b^* = 1.36$ as derived in Li *et al.* (2022) (see their appendix A).

3. Numerical set-up and boundary conditions

The present study focuses on the experiment of Irschik *et al.* (2004), where waves propagate on a 1 : 10 sloped bed and break on the frontline of a vertical pile with its centre located at the end of the slope. The circular pile has diameter $D = 0.7$ m. The layout of the numerical set-up, following the experimental study of Irschik *et al.* (2004), is presented in figure 1. The origin of the coordinate system is set at the centre of the pile at the undisturbed free surface. Waves are generated at the left end of the tank and propagate in the x direction. The y axis points in the transverse direction. The width of the flume is 5 m with the pile installed in the middle between the two sides. Following the experiment of Irschik *et al.* (2004), the wave period is $T = 4.0$ s and the incident wave height is $H = 1.3$ m. For the given wave conditions, the surf similarity parameter is calculated as

$$\xi_0 = \frac{\tan\beta}{\sqrt{H_0/L_0}}, \tag{3.1}$$

where $\tan\beta = 1/10$ is the slope, $L_0 = gT^2/(2\pi)$ is the deep-water wavelength and

$$H_0 = H\sqrt{\tanh(k_w h)\left(1 + \frac{2k_w h}{\sinh(2k_w h)}\right)} \tag{3.2}$$

is the deep-water wave height calculated according to linear wave theory, and k_w is the wavenumber at the paddle depth $h = 3.8$ m. This yields $\xi_0 = 0.42$, corresponding to an expected strong spilling breaking scenario ($\xi_0 < 0.5$).

Based on our preliminary grid convergence study, the number of cells used per incident wave height is $H/\Delta z = 30$, combined with $\Delta x = \Delta y = 1.5\Delta z$, corresponding to approximately 322 grid cells per wavelength at the paddle depth. For the numerical schemes, a second-order interpolation scheme is used for divergence terms, e.g. the convection terms. The maximum Courant number is set as $Co = 0.05$ to ensure that the simulation is stable and with accurate velocity fields, in accordance with the discussion in Larsen *et al.* (2019).

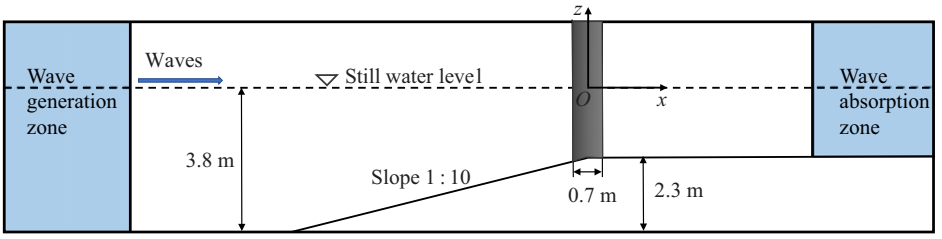

Figure 1. The layout of the present numerical set-up.

The boundary conditions are set as follows: (1) At the inlet a wave generation zone is utilized, where waves are specified with a numerically exact streamfunction solution (Fenton 1988), utilizing the waves2foam toolbox (Jacobsen, Fuhrman & Fredsøe 2012). (2) At the outlet a wave absorption relaxation zone is utilized to minimize reflection. (3) The pile surface, tank bottom and two tank sides are set as non-permeable smooth walls with zero velocity (i.e. no slip condition) and zero normal gradient of the pressure. A standard smooth wall function for ω is applied. (4) The top of the domain is the air. The interface between the air and the water is the free surface that is tracked with a volume fraction coefficient α ($\alpha = 1$ for water, $\alpha = 0$ for air and any value in between indicates a fluid mixture).

4. Prediction of the breaking point

4.1. *Influence of the turbulence closure models*

The study of Qu *et al.* (2021) suggests that the choice of turbulence model will affect the breaking point relative to the pile. In this section we will therefore reinvestigate the influence of the turbulence model on the breaking point using a small Courant number (i.e. $Co = 0.05$) and second-order accuracy of discretisation schemes. This again ensures good numerical accuracy in both free surface elevations and velocity kinematics, following Larsen *et al.* (2019). In the next subsection we will discuss the effect of the Courant number on the breaking point. To investigate the influence of turbulence models on the breaking point in a cost-effective manner, we first remove the monopile at the end of the slope. Four 2-D simulations involving waves propagating up the 1 : 10 slope are performed with (1) no turbulence model, (2) the Wilcox (2006) k–ω model, (3) the LF18 k–ω model and (4) the Wilcox (2006) stress–ω model.

Figure 2 presents the wave profiles and turbulence levels when the waves just begin to break at the location of the pile frontline (the pile location is added merely as a reference). The time instant is at $t/T = 4.25$ when the waves have reached repeatable (periodic) status. It is interesting to see that using $Co = 0.05$ and second-order schemes, the progressive waves break at the same location regardless of the turbulence model (indeed, even with no turbulence model). This contradicts Qu *et al.* (2021), but is in line with our own physical expectations: before wave breaking, there should be no significant turbulence production beneath the free surface, apart from the very thin boundary layer region near the bed (also evident in figure 2). Therefore, a laminar model (i.e. no turbulence model) should be able to accurately predict the wave profiles up to the onset of breaking. In the meantime, it should be expected that from wave shoaling on the slope to breaking on the cylinder front, the simulation with using an accurate (and stable, L18 k–ω) turbulence model should behave very similar to that without a turbulence model. In short, the breaking point should not be

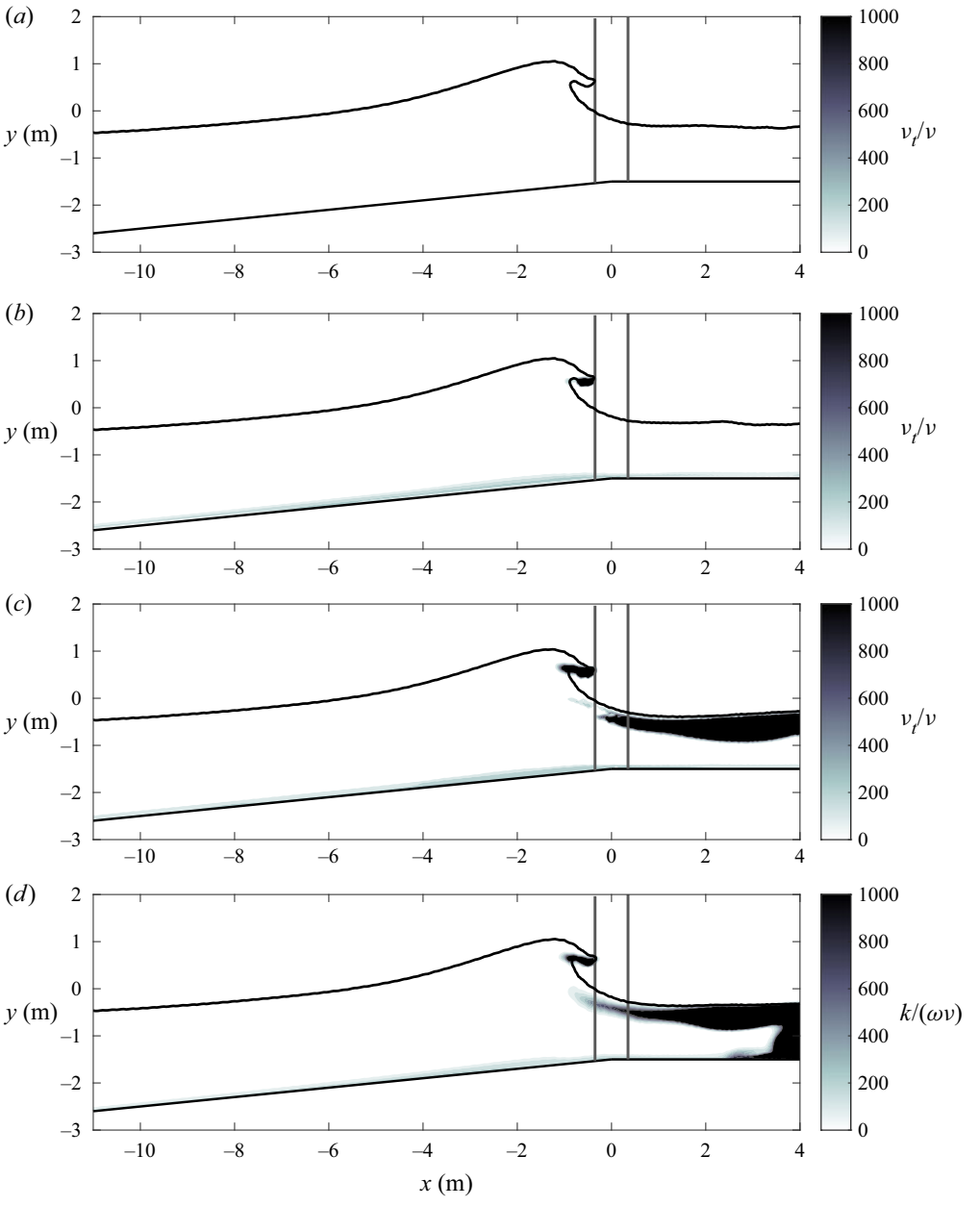

Figure 2. Wave profiles and turbulence levels when the waves are breaking right at the location where the frontline of the monopile is located with (*a*) no turbulence model, (*b*) Wilcox (2006) *k*–ω model, (*c*) LF18 *k*–ω model, (*d*) Wilcox (2006) stress–ω model. The time instant is $t/T = 4.25$ when the waves reached repeatable status. (Note that (*d*) is plotted with $k/(\omega\nu)$ as the stress–ω model does not utilize the eddy-viscosity assumption; this expression is comparable to ν_t/ν for two-equation models.) (*a*) No turbulence model, $Co = 0.05$. (*b*) Wilcox (2006) *k*–ω model, $Co = 0.05$. (*c*) The LF18 *k*–ω model, $Co = 0.05$. (*d*) Wilcox (2006) stress–ω model, $Co = 0.05$.

altered by the choice of turbulence model if a stable turbulence model is properly applied and the simulation is converged. This is clearly demonstrated in figure 2.

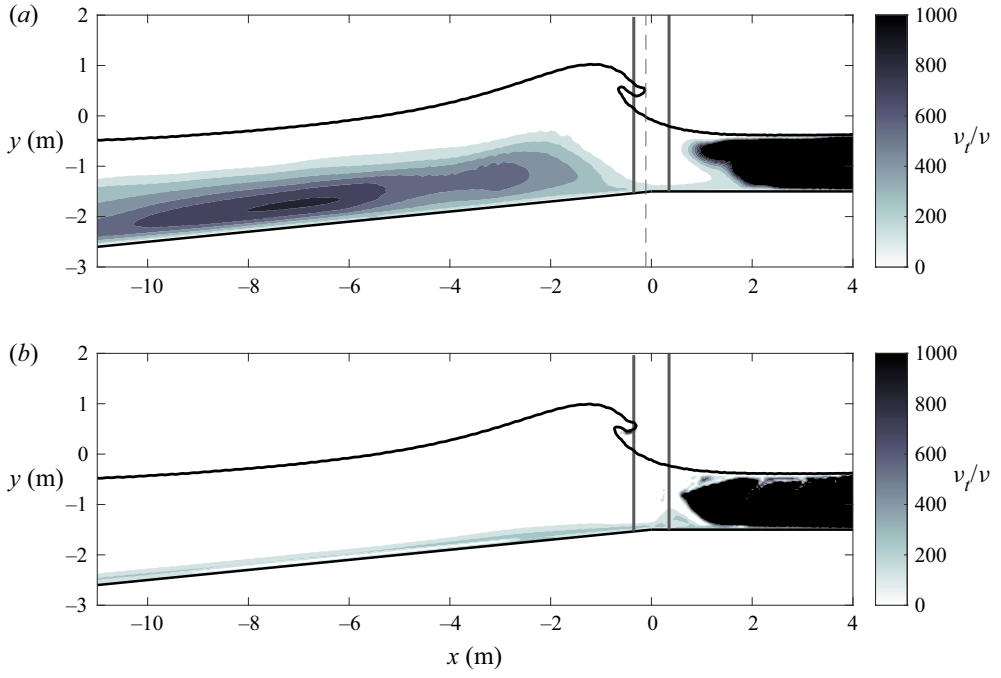

Figure 3. Wave profiles and turbulence levels with (*a*) the Wilcox (2006) *k–ω* model and (*b*) the LF18 *k–ω* model at the time instant $t/T = 50.25$. In (*a*) the vertical dashed line indicates the breaking point. (*a*) Wilcox (2006) *k–ω* model, $Co = 0.05$. (*b*) The LF18 *k–ω* model, $Co = 0.05$.

Note that figure 2 is at an early time instant after waves reach a repeatable status. At this early time, the turbulence over-production with the Wilcox (2006) *k–ω* model (figure 2*b*) has not yet grown to a significant level. If we further run the simulations to over 50 wave periods, an obvious instability of the Wilcox (2006) *k–ω* model can be seen. Figure 3(*a*) further presents results at a time instant $t/T = 50.25$, computed with the Wilcox (2006) *k–ω* model. It is shown that turbulence level has now largely increased in the pre-breaking region. This over-production of turbulence extracts energy from the propagating waves and decays the wave amplitude, thus causing the waves to gradually break later than in figure 2. As indicated by the dashed line in figure 3(*a*), the wave breaking point is behind the location of the pile frontline. This problem does not exist with the LF18 *k–ω* model (because of the stabilization), as shown in figure 3(*b*), where the turbulence at the pre-breaking region is kept small and the breaking point remains accurately on the pile frontline even after 50 wave periods. Similar results as in figure 3(*b*) have been achieved with the stress–*ω* model (because the model is neutrally stable), as well as with the no turbulence model; they are not shown here for the sake of brevity. A similar comparison and discussion can also be found in Larsen & Fuhrman (2018) and Li *et al.* (2022).

If we place the vertical pile in the tank, the same results can be reached, i.e. we find that the presence of the pile does not significantly alter the incipient breaking point. Figure 4 presents a screen shot for the 3-D simulation including the pile with waves initially breaking on the front surface of the pile. The simulation in figure 4 is performed with the stress–*ω* model at $t/T = 8.25$ after waves reach a repeatable state. The fluid domain is coloured with the turbulent kinetic energy *k*. The red zone after breaking indicates high turbulent kinetic energy, while the blue zone prior to breaking indicates low turbulent

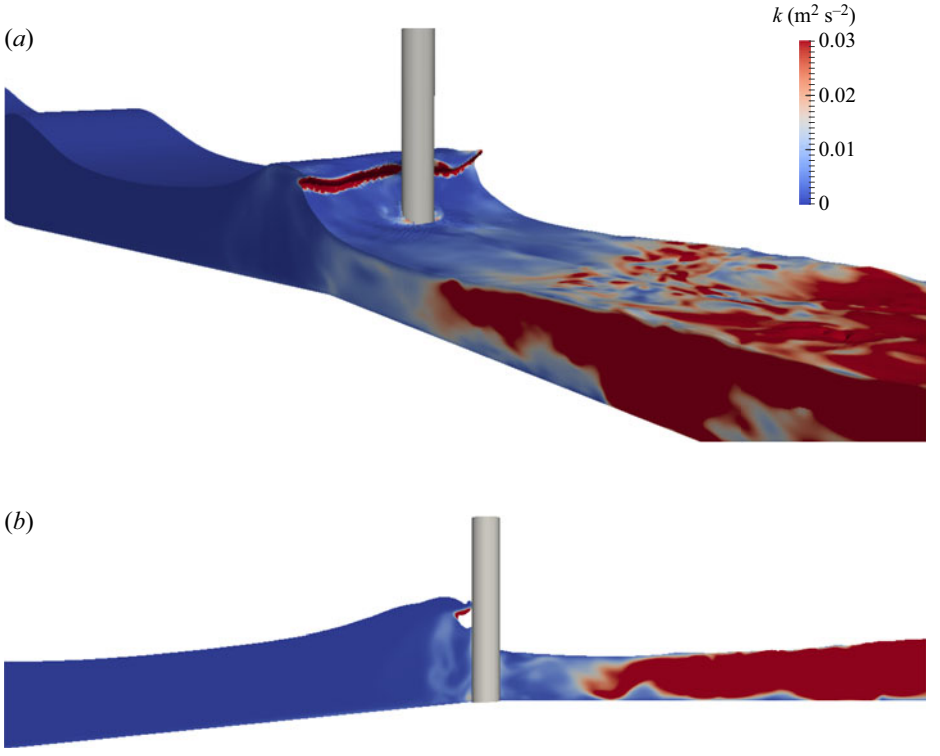

Figure 4. Screenshots of the 3-D simulation of waves breaking exactly on the vertical pile frontline at $t/T = 8.25$, simulated with the Wilcox (2006) stress–ω model. (*a*) A 3-D view at the breaking instant. (*b*) Centre section ($y = 0$) view at the breaking instant.

kinetic energy. Similar scenarios have been observed using the LF18 k–ω model and other models, which are not shown here for brevity.

4.2. *Effect of the Courant number*

In this section we will further investigate the effect of the Courant number on the predicted breaking point. Figure 5 presents the 2-D breaking wave simulations (again, without the presence of the vertical pile) with the stress–ω model and with Co ranging from 0.025 to 0.3. Figure 5(*a*,*b*) shows that with $Co = 0.025$ and 0.05, the breaking point is on the frontline of the vertical pile, which is the same as that observed in the experiment (Irschik *et al.* 2004) with the same wave condition and slope. This indicates that the breaking point is reasonably converged with $Co \leq 0.05$. However, as Co is increased to 0.1 and larger, as shown in figure 5(*c*–*e*), the waves break earlier and earlier. Larsen *et al.* (2019) demonstrated that for non-breaking wave simulations in OpenFOAM with the VOF method and PIMPLE algorithm (a combination of PISO – pressure implicit with splitting of operator – and SIMPLE – semi implicit method for pressure-linked equations), there is a tendency for surface elevations to increase and crest velocities to become severely overestimated, even over relatively short times. They found that a relatively small Co is required to mitigate this problem. This implies that many past simulations may not have converged velocity kinematics, especially near the crest. The present study on breaking waves has demonstrated a similar phenomenon as the study on non-breaking progressive waves in Larsen *et al.* (2019). It is hence found that a large Co can alter the breaking point

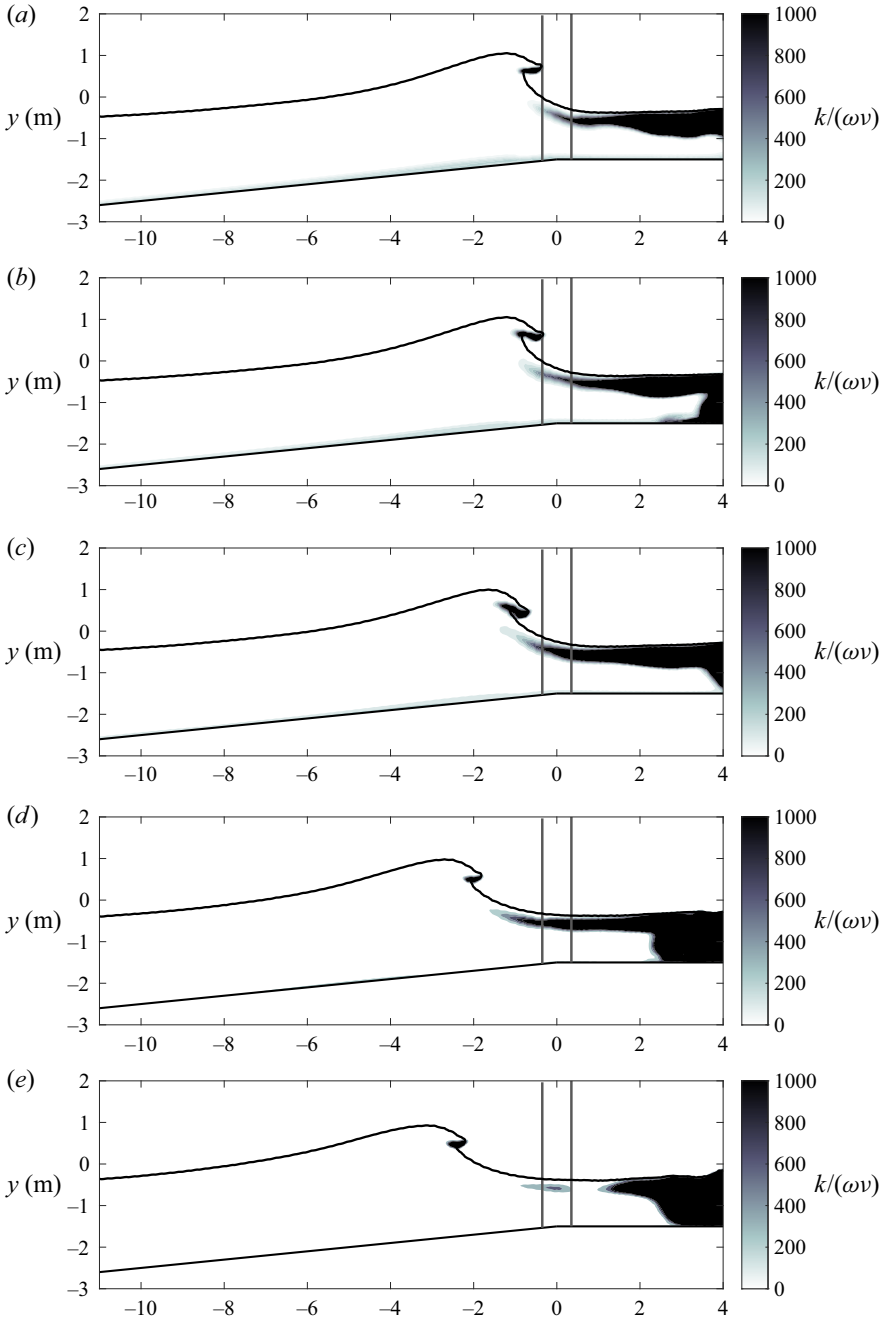

Figure 5. Computed wave profiles and turbulence levels at incipient breaking utilizing the Wilcox (2006) stress–ω model with various Co. Note that the case with $Co = 0.05$ is a repeat of that shown in figure 2(d). Results are shown for (a) $Co = 0.025$, (b) $Co = 0.05$, (c) $Co = 0.1$, (d) $Co = 0.2$, (e) $Co = 0.3$.

due to inaccurate flow kinematics, whereas maintaining $Co \leq 0.05$ can ensure reasonable convergence in the breaking position.

Interestingly, if a large Co is used together with a two-equation turbulence model that is unstable in the potential flow region beneath waves (e.g. the standard k–ω model, the

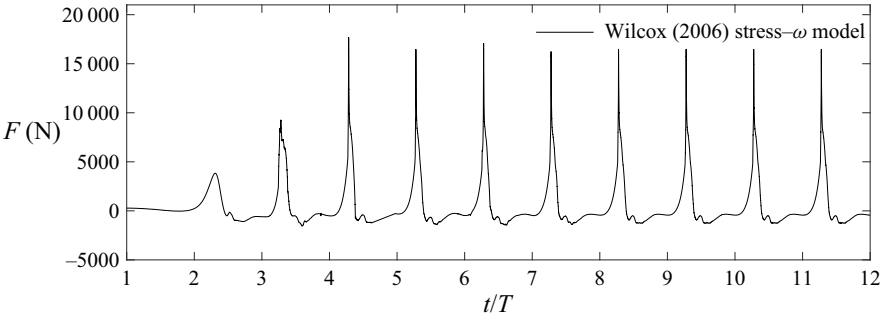

Figure 6. The time series of the total horizontal in line force predicted with the Wilcox (2006) stress–ω model.

standard realizable k–ε model, which has a tendency of turbulence over-production), the two errors could cancel each other, i.e. early breaking due to a large Co may be delayed due to decreasing wave heights caused by the turbulence over-production and associated unphysical energy dissipation. In this way the waves may coincidentally break on the pile, but the waves would expectedly have both a polluted turbulence field and inaccurate velocity kinematics. This is what we believe occurred in the simulation of Qu *et al.* (2021): their simulation with $Co = 0.5$ and the standard k–ω SST model showed that their waves broke right on the pile frontline after 40 wave periods, but their domain was clearly polluted by turbulence over-production prior to breaking (see their figure 11*d*).

5. Prediction of breaking wave forces on the pile

Section 4 shows that a proper use of the turbulence model (either a stabilized two-equation model such as the LF18 k–ω model or a neutrally stable Reynolds stress model such as the stress–ω model) and a small Courant number can lead to an accurate prediction of the breaking point. In this section we will proceed specifically with these two models (and with no turbulence model as a reference) to perform quantitative investigations on the hydrodynamic forces exerted on the vertical pile by the breaking waves. The peak force and the SLC will be investigated and compared between the selected models. As we showed earlier (figure 3), standard two-equation models, e.g. the Wilcox (2006) k–ω model, have the inherent instability problem (unphysical exponential growth of the turbulent kinetic energy) beneath progressive waves, thus, they are excluded from the present section. The present 3-D simulations are performed for 12 wave periods. The surface elevation and forces computed with the selected turbulence models in the presence of the structure reach a periodic state from approximately the seventh wave period, as shown in figure 6. (In what follows, we define $t/T = 0$ at the beginning of the seventh wave period.) Note that the 3-D simulations with a pile reach the periodic state slightly later than the 2-D simulations without a pile in § 4 where waves are repeatable from the fourth wave period. With the presence of the structure, the grid cells near the pile surface are further refined with the distance from the first cell centre to the cylinder surface of $0.011D$, which is equivalent to $0.12\Delta x$, i.e. around ten times smaller than the cell size along the wavelength in the 2-D simulations. This cell size is maintained in the area within a distance D to the pile surface. The 3-D simulation with the stress–ω model required approximately one month to run in parallel on 64 processors on the supercomputing cluster at the Technical University of Denmark. The total computational time using the k–ω model is approximately 15 % less than with the stress–ω model.

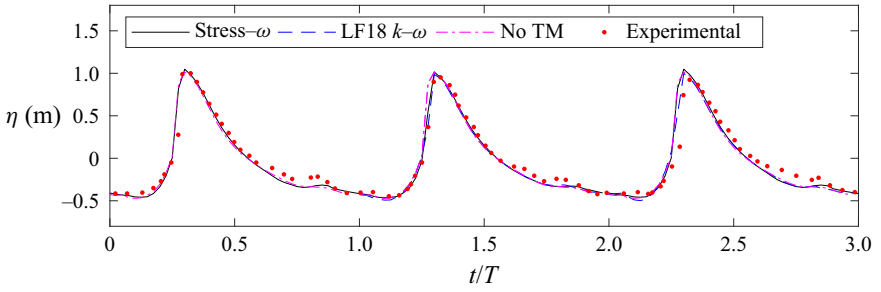

Figure 7. Comparison of computed and measured (Irschik *et al.* 2004) surface elevations at $(x, y) = (-0.7\,\mathrm{m},\ 1.9\,\mathrm{m})$. Here $t/T = 0$ is defined at the seventh wave cycle when the simulation reaches a repeatable state (similarly on several forthcoming figures). In the legend, TM stands for turbulence model.

5.1. *Peak load cycle*

Before comparing the forces, the time series of the surface elevation near the vertical pile are presented in figure 7 to validate the simulated waves. The surface elevation at $(x, y) = (-0.7\,\mathrm{m},\ 1.9\,\mathrm{m})$ was measured in Irschik *et al.* (2004) and presented in Choi *et al.* (2015). Figure 7 shows the numerically predicted (i.e. with the Wilcox (2006) stress–ω model, the LF18 k–ω model and no turbulence model) and the experimentally measured surface elevation η. A good match is observed between all three numerical predictions and the experimental data. As no turbulence is produced before wave breaking, the results with the turbulence models are essentially the same as without. This further confirms that the choice of turbulence model should not affect the accuracy of wave-induced surface elevations before wave breaking.

The peak force F (i.e. the total horizontal force in the x direction) induced by breaking waves on the vertical pile is presented in figure 8. Numerical predictions with the Wilcox (2006) stress–ω model, the LF18 k–ω model and no turbulence model are compared with the processed experimental data presented in Choi *et al.* (2015). It is noted that the forces measured in the original experiments of Irschik *et al.* (2004) were recorded synchronously with a sampling rate of 200 Hz. In order to eliminate the amplified force component due to the structural vibration that was recorded in the experiment, Choi *et al.* (2015) applied a low-pass filter of 20 Hz to cutoff the signal at the structural natural frequency and used the empirical mode decomposition (EMD, by taking the mean of the upper and lower signal envelope) to separate the net breaking wave force from the measured data. Figure 8 compares the processed (with both the low-pass filter and EMD) experimental data presented by Choi *et al.* (2015) with the present numerical results. In figure 8, $t_D \approx 0.02T$ is the duration of the sharp peak (or slamming force). It is seen that all three numerical simulations can predict the slamming duration reasonably in line with the measurement. However, it is noted that the numerical predictions of the peak force are generally higher than the processed experimental data. This might be due to the EMD applied in Choi *et al.* (2015) to process the experimental data that significantly reduced the peak value. Figure 9(*a*) alternatively compares the computed force results from all three models with the low-pass filtered experimental force from Choi *et al.* (2015), without EMD. It can therefore be seen that the peak experimental force (approximately 1.8×10^4 N) matches quite well with those computed (e.g. 1.6×10^4 N, as predicted with the stress–ω model). Both of these values are above the experimental peak (1.2×10^4 N) when both low-pass filtering and EMD are applied. In figure 9(*b*) we additionally compare the numerical results from the stress–ω model (black line) with both the unfiltered (raw)

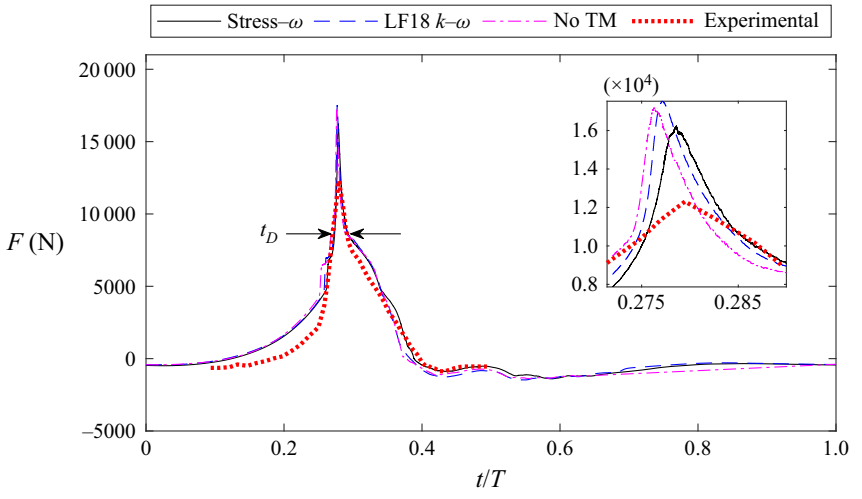

Figure 8. Instantaneous peak force from the present numerical predictions and the measured data processed in Choi *et al.* (2015) with a low-pass filter and empirical mode decomposition (EMD).

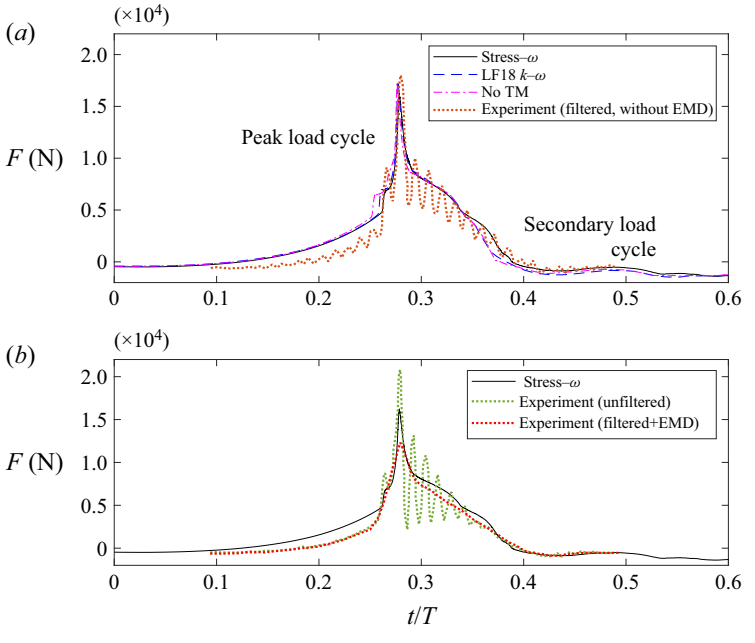

Figure 9. Comparison of forces among selected numerical predictions and (*a*) the filtered experimental force without EMD and (*b*) the raw experimental force and after application of both filter and EMD. All experimental data are from Choi *et al.* (2015).

force signal (digitized from Choi *et al.* (2015), green dotted line) and the same signal after application of low-pass filtering and EMD (red dotted line, as in figure 8). It can be seen in figure 9(*b*) that the peak force computed with the stress–ω model is in between the raw (unfiltered) and the processed (low-pass filter and EMD) peaks. Based on the comparisons in figure 9, and the differences in the model (fixed monopile) versus that used in the experiment, the computed peak force appears reasonable. It is likewise clearly seen from figure 9 that during the rise leading up to the peak ($t/T < 0.25$), and also

during the SLC ($t/T > 0.4$), neither the low-pass filter or EMD affect the force amplitude significantly. Therefore, in the discussion of SLC that follows, we adopt the processed (i.e. both low-pass filtered and EMD) experimental force signal for comparison. Note that this processed experimental data are available for a longer time duration during the SLC, as presented in Jose *et al.* (2017).

Another common feature that can be noted for all three numerical results is that they predict an almost identical rise leading up to the peak force and more or less the same peak value. This is again because the peak force is measured right at the onset of wave breaking. From pre-breaking up to the breaking onset, we expect that even with no turbulence model, the peak force should be accurately predicted, as argued above. Our numerical results are in line with this expectation. This draws an unsurprising, but apparently new, conclusion, that a proper application of turbulence models should not alter the numerical prediction of the peak force when waves incipiently break right on the frontline of a vertical cylinder. Indeed, no previous studies have shown this result (likely due to the large Courant number and/or unstable turbulence models utilized). However, it is emphasized that this conclusion is only valid for cases where waves initially break right on the structure. If a wave breaks prior to reaching the structure, a turbulence model must be used to predict the wave force on the structure, as this becomes a post-breaking problem and breaking-induced turbulence will have been produced. It is also worthwhile to mention that to reach convergence, $Co = 0.05$ is applicable for wave simulations using the VOF method, ensuring good accuracy in the velocity field beneath the surface. This may not be a universal criterion for all kinds of RANS-based simulations, however.

5.2. *Secondary load cycle*

Following the peak force, a SLC occurs for the present case. The predicted SLC is compared with the experimental data in figure 10. It is seen that the numerical predictions in each subfigure reasonably capture the duration of the SLC, defined according to Chaplin *et al.* (1997) as the horizontal time span from points A to B in each subfigure, corresponding to approximately 11 % of the wave period. The amplitude of the SLC is defined as the vertical force difference between points C and D. The numerical predictions of the so-called SLC ratio, i.e. the SLC load divided by the numerical peak force, are around 3 % for all the numerical predictions. Previous experimental studies, e.g. Grue *et al.* (1993), have reported amplitudes of the SLC up to 11 % of the peak force. The present numerical predictions are below this value.

Although the numerical predictions with all three models seem to be able to reasonably capture the SLC load and duration, figure 10(*b*) shows an obvious magnitude difference of the force during the SLC between the LF18 k–ω prediction and the experimental data (almost double in the minimum force). The no turbulence model prediction of the force magnitude during the SLC in figure 10(*c*) is somewhere in between the numerical results in figure 10(*a*,*b*). Figure 10(*a*) presents a good match between the stress–ω model prediction and the measurement of the force magnitude during the SLC.

To provide an in-depth look of each simulation on the SLC, turbulence characteristics around the pile are investigated as follows. We have concluded earlier that the accurate peak force prediction is essentially independent of the turbulence model utilized. However, as the SLC is generated after wave breaking and is associated with the flow around the cylindrical body, turbulence models are expected to have a more significant effect on the SLC predictions. Figure 11 shows the vorticity field at $z = -D/2$ at $t/T = 0.49$, when the SLC reaches its local peak (see figure 10). It is seen that with the stress–ω model in figure 11(*a*), a strong vortex pair is formed in the lee-wake of the pile. Vortex shedding does

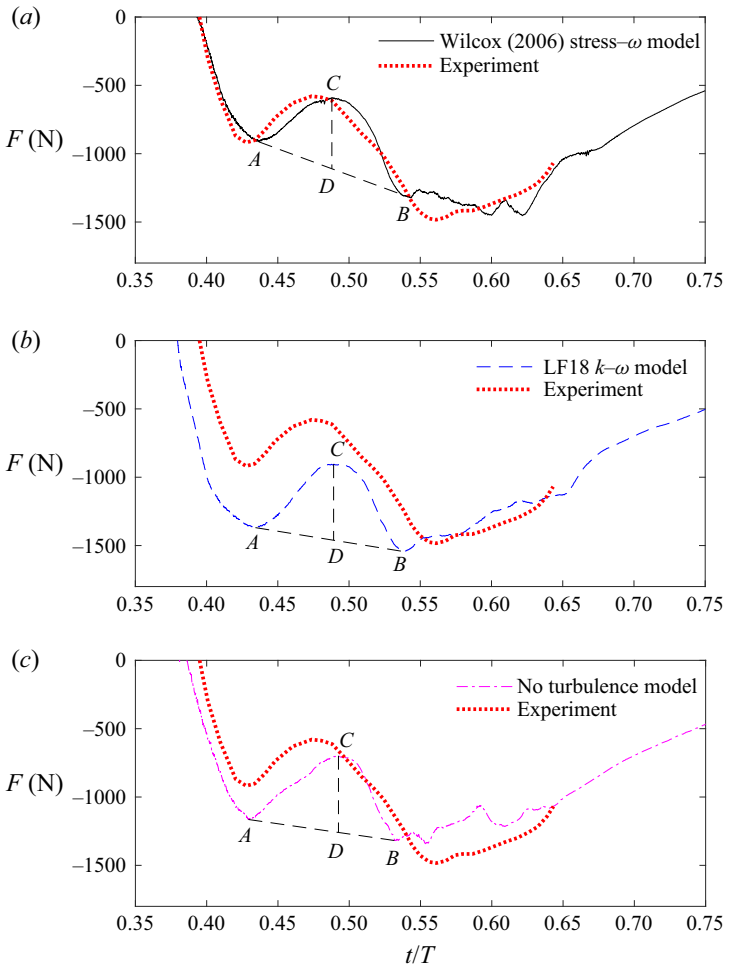

Figure 10. Secondary load cycle by numerical predictions and the experimental measurement.

not occur for this condition, as the Keulegan–Carpenter number ($KC = U_m T/D$, where U_m is the amplitude of the flow velocity oscillation) is small with $KC \approx 6$ at $z = -D/2$, such that the flow changes direction prior to vortices being shed. A detailed discussion of KC and the vortex shedding can be found in Li *et al.* (2020). The prediction with the LF18 k–ω model in figure 11(b) shows a weaker vortex pair attached to the pile. However, when predicting with no turbulence model, as shown in figure 11(c), the flow separation and vortex field are completely different. We expect this result is wrong as it would be necessary to refine the computational mesh and the time step to a DNS simulation level to ensure the turbulence is resolved, which is not practical for the present 3-D wave–structure interaction case. The simulation with no turbulence model in the present study utilizes the same mesh as with turbulence models on. Therefore, in the turbulent region, the turbulence is not solved in a physically correct manner. Thereby, the simulation with no turbulence model is dropped in the following analysis. When comparing figures 11(a) and 11(b), a stronger vorticity field is predicted with the stress–ω model, which in turn causes larger magnitude negative pressure on the lee side during the flow reversal. This generates a

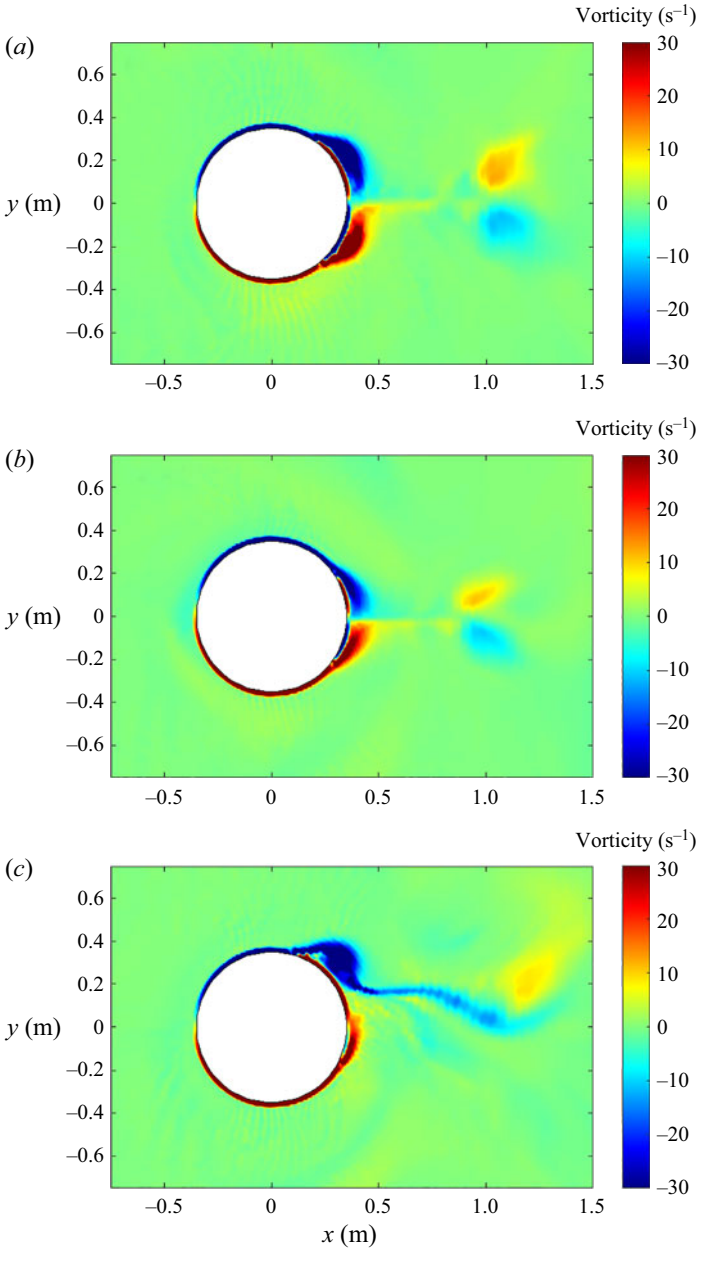

Figure 11. Vorticity field with (*a*) the Wilcox (2006) stress–ω model, (*b*) the LF18 k–ω model and (*c*) no turbulence model at $z = -D/2$ and time instant of t/T=0.49, i.e. the local peak of the SLC.

stronger suction force on the lee side and raises the total horizontal force up in figure 10(*a*), which matches much better with the measurement.

Figure 12 further presents the 3-D coherent vortical structures identified by the Q criterion simulated with the stress–ω model and the LF18 k–ω model. The Q criterion (Dubief & Delcayre 2000) is the second invariant of the velocity gradient tensor, which is

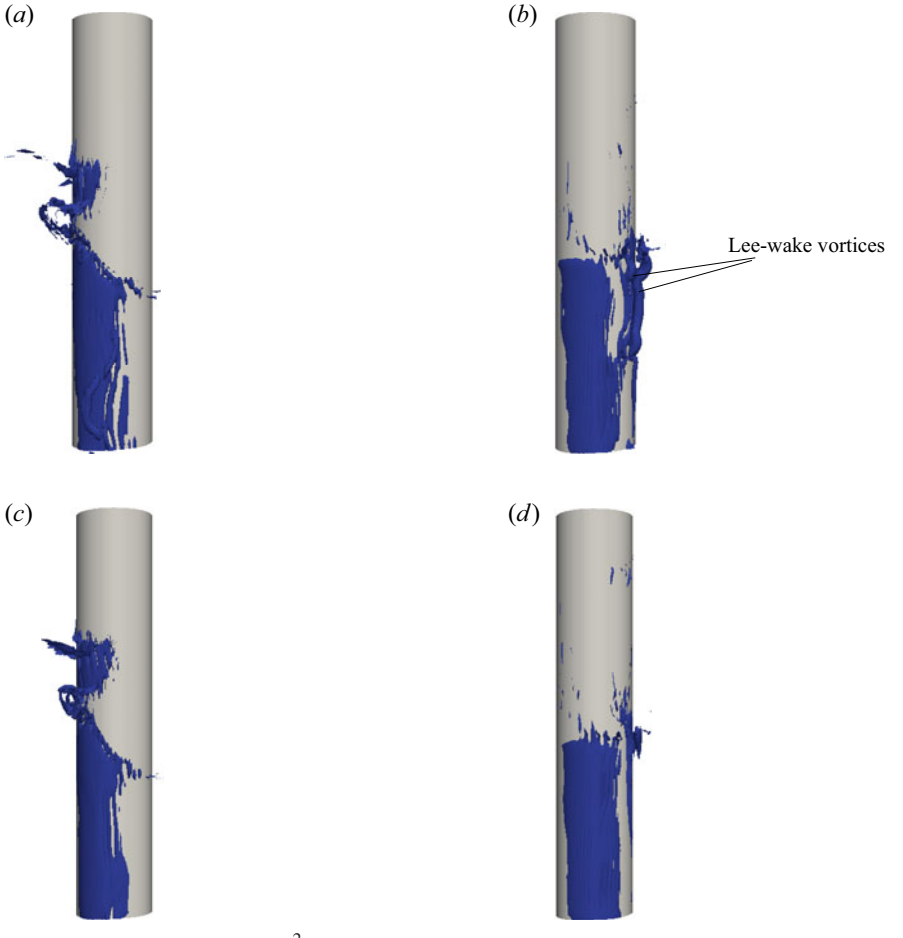

Figure 12. Instantaneous $Q = 200\,\mathrm{s}^{-2}$ isocontours in the vicinity of the vertical pile at the wave breaking instant and the local peak of SLC. Results are shown for (*a*) $t/T = 0.28$, Wilcox (2006) stress–ω model; (*b*) $t/T = 0.49$, Wilcox (2006) stress–ω model; (*c*) $t/T = 0.28$, LF18 k–ω model; (*d*) $t/T = 0.49$, LF18 k–ω model.

defined as

$$Q = \frac{1}{2}\left(S_{ij}^2 - \Omega_{ij}^2\right). \tag{5.1}$$

Instantaneous isosurfaces corresponding to $Q = 200\,\mathrm{s}^{-2}$ in the water phase are shown in figure 12 at two time instants, i.e. when the waves are just breaking on the pile front ($t/T = 0.28$) and when the SLC reaches its local maximum ($t/T = 0.49$). The isosurfaces shown in figure 12(*a*) with the Wilcox (2006) stress–ω model and 12(*c*) with the LF18 k–ω model are similar at the wave breaking instant. The slight temporal difference is due to minor model differences. However, comparing figures 12(*b*) and 12(*d*) at the SLC local peak, obviously different structures are observed in the lee wake of the pile. Figure 12(*b*) with the stress–ω model predicts the pair of lee-wake vortices that were also shown in the DNS study of Jang *et al.* (2021) at $KC = 6$ (though in that study waves were simplified to oscillatory flows without considering the free surface). It is also noted that the formed vortex pair are tilting toward the bottom because of the boundary layer effect

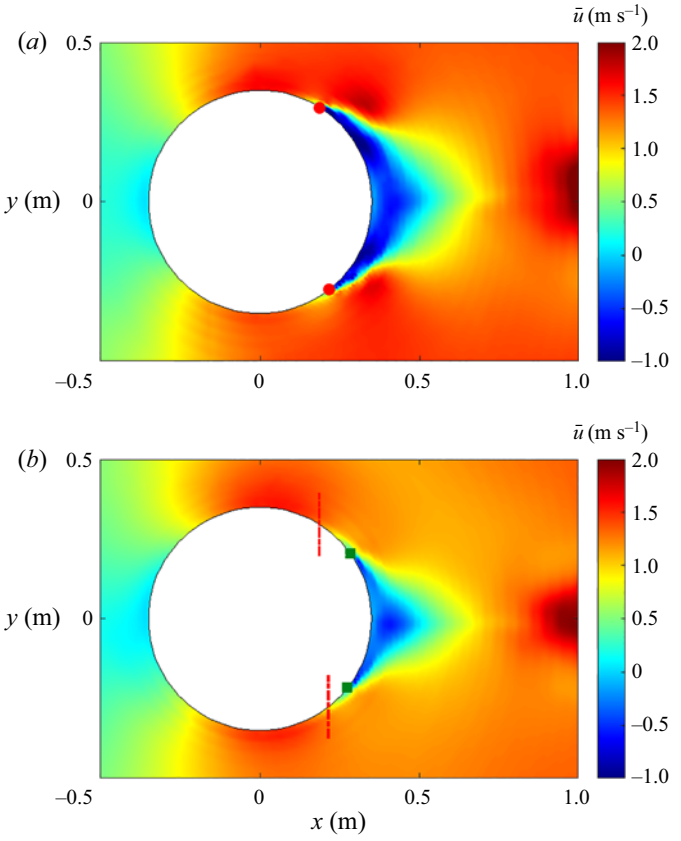

Figure 13. Horizontal velocity field with (*a*) the Wilcox (2006) stress–ω model and (*b*) the LF18 k–ω model at $z = -D/2$ and the time instant of t/T=0.49, i.e. the peak of the SLC. In each subfigure red dots indicate the separation points from the Wilcox (2006) stress–ω model and green squares from the LF18 k–ω model. The red dashed lines in (*b*) indicate the locations of separation points projected from (*a*).

near the bottom wall. However, the isosurfaces simulated with the LF18 k–ω model do not demonstrate this feature; the lee-wake vortices were not clearly formed.

The differences in the vorticity field and the vortex formation are strongly linked to the flow separation. Figure 13 presents the horizontal velocity field $\bar{u}$ and compares the separation points for the Wilcox (2006) stress–ω model and the LF18 k–ω model. The separation point is defined as the point where the wall shear stress becomes zero, i.e. $(\partial u/\partial n)|_{wall} = 0$. In each subfigure the red dots indicate the separation points from the stress–ω model and green squares from the LF18 k–ω model. It is observed that the flow separates further downstream with the LF18 k–ω model. This indicates that the simulated flow is more turbulent with the LF18 k–ω model than with the Wilcox (2006) stress–ω model. A simple explanation for this is that the more turbulent boundary layer has greater mixing of momentum with the outer flow, thus delaying the separation. A closer look at the turbulence field near the boundary of the pile is presented in figure 14 at $z = -D/2$. It is seen that as flow travels from the upstream point along the pile surface, the turbulent kinetic energy k around the pile is indeed higher when predicted with the LF18 k–ω model than with the stress–ω model. Well-known shortcomings associated with the two-equation model, e.g. that the turbulence field near the curved surface is

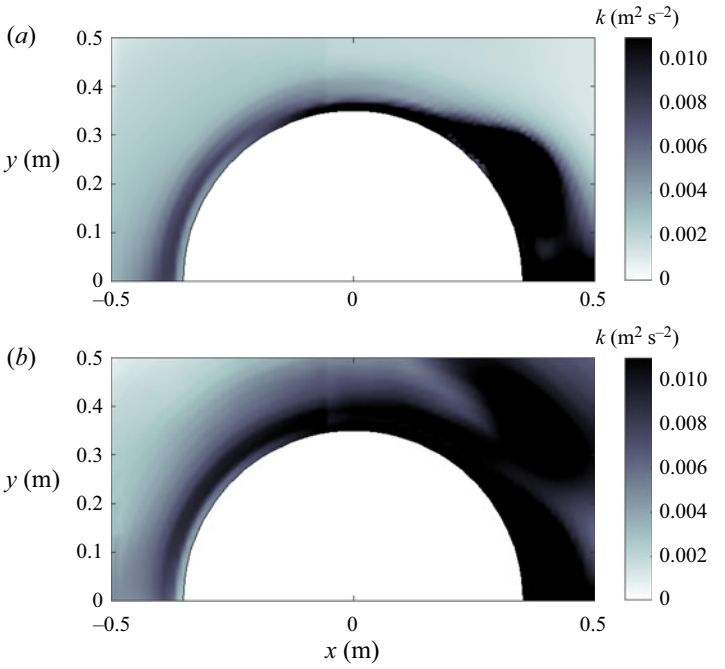

Figure 14. Turbulent kinetic energy around the pile at $z = -D/2$ and the time instant of $t/T = 0.49$, simulated with (*a*) the Wilcox (2006) stress–ω model and (*b*) the LF18 k–ω model.

not accurately predicted, lead to later separation points and further underestimated vortex strength on the lee side.

It can be seen from the discussion above that as the SLC is generated after wave breaking, it is closely associated with the flow around the cylindrical body. Thus, accurate turbulence modelling has a significant effect on the SLC predictions. Although some existing studies have claimed that the SLC is not necessarily linked to the flow separation (e.g. Grue *et al.* 1993; Ghadirian & Bredmose 2020), the flow separation point does affect the SLC amplitude when it occurs. Therefore, accurate turbulence modelling is seemingly required to predict the SLC. The present study demonstrates the advantage of using the stress–ω model, which breaks free from the traditional Boussinesq approximation for this purpose. Therefore, this model is able to predict both the peak and SLCs accurately.

6. Conclusions

The present work has focused on the turbulence modelling of incipient wave breaking on a vertical circular pile on a sloped bed. In the present study we have first investigated the effects of the turbulence model and the Courant number (Co) on the breaking point. We showed that the breaking point is not affected by turbulence modelling, as long as the turbulence model is stable in the potential flow region (e.g. the LF18 k–ω model (Larsen & Fuhrman 2018) and the Wilcox (2006) stress–ω model) and the simulations are converged (with sufficiently small Co). We showed that simulations with $Co \leq 0.05$ can reach a converged breaking point, while $Co \geq 0.1$ can cause an obviously early breaking due to inaccurate velocity kinematics. Additionally, due to their instability (Larsen & Fuhrman 2018; Fuhrman & Li 2020), two-equation models in their standard forms (e.g. the

Wilcox (2006) k–ω model, the k–ω SST model, the realizable k–ε model) may lead to turbulence over-production and associated wave decay, thus delaying breaking. It it noted that if a large Co is used together with a standard two-equation turbulence model, these two errors may cancel each other, and waves may break at a desired location, but polluted with a non-physical turbulence field. We believe this is what has occurred in the study of Qu *et al.* (2021), who showed that the standard k–ω SST model with $Co = 0.5$ leads to an 'accurate' breaking location, but clearly coupled with such an unphysical turbulence field. Their work also showed that the stabilized k–ω SST model leads to early breaking, which in light of the present study seems clearly due to the large $Co = 0.5$ used in their simulations.

The present study has then investigated breaking wave forces on a vertical cylinder based on the experiment of Irschik *et al.* (2004) with the Wilcox (2006) stress–ω model (as used previously in breaking wave simulations of Li *et al.* 2022), the stabilized LF18 k–ω model and no turbulence model, all with low $Co = 0.05$ and second-order discretization schemes. It has been shown that the peak force on the vertical cylinder is not affected by the choice of turbulence model (again, as long as the turbulence model is stable and the simulations are converged). Specifically, up to the onset of breaking where the incipient peak force occurs, accurate predictions can be achieved even without a turbulence model.

However, the prediction of the SLC requires proper turbulence modelling, as the process is post-breaking and involves turbulence production and lee-side flow separation. Compared with the LF18 k–ω model, the Wilcox (2006) stress–ω model has shown a more accurate prediction of the SLC, as the flow separation points and the vortical field in the lee wake are predicted with better accuracy. Although some existing studies indicated that the generation of the SLC does not require flow separation, but is rather mainly due to the pressure-induced suction force, it has been shown in the present work that the flow separation point significantly affects the pressure field in the lee wake and can hence further affect the suction force and the SLC magnitude. For waves breaking on a vertical pile, accurate turbulence modelling is thus essential for the SLC predictions. Overall, the Wilcox (2006) stress–ω model has been proved capable of providing good accuracy for the full processes, i.e. during wave propagation on the sloped bed, to breaking on the vertical pile and the induced peak force, and all the way to the flow separation, lee-wake vortex formation and the SLC.

Funding. The first author gratefully acknowledges financial support from the European Union's Horizon 2020 research and innovation program, Marie Sklodowska-Curie grant no. 713683 (COFUNDfellowsDTU, H.C. Ørsted Postdoc project SUBSEA: SimUlating Breaking waves and SEdiment trAnsport with stabilized turbulence models). The second author gratefully acknowledges financial support from the Independent Research Fund Denmark (projects SWASH – simulating wave surfzone hydrodynamics – and sea bed morphology, grant no. 8022-00137B and STORM – statistics and forces on structures from extreme – water waves in finite depth, grant ID: 10.46540/2035-00064B). This support is greatly appreciated.

Declaration of interests. The authors report no conflict of interest.

Author ORCIDs.
Yuzhu Li https://orcid.org/0000-0002-3650-6551;
David R. Fuhrman https://orcid.org/0000-0002-2433-6778.

References

Antolloni, G., Jensen, A., Grue, J., Riise, B.H. & Brocchini, M. 2020 Wave-induced vortex generation around a slender vertical cylinder. *Phys. Fluids* **32** (4), 042105.

Apelt, C.J. & Piorewicz, J. 1987 Laboratory studies of breaking wave forces acting on vertical cylinders in shallow water. *Coast. Engng* **11** (3), 263–282.

BIHS, H., KAMATH, A., CHELLA, M.A. & ARNTSEN, Ø.A. 2016 Breaking-wave interaction with tandem cylinders under different impact scenarios. *ASCE J. Waterway Port Coastal Ocean Engng* **142** (5), 04016005.

BROWN, S.A., GREAVES, D.M., MAGAR, V. & CONLEY, D.C. 2016 Evaluation of turbulence closure models under spilling and plunging breakers in the surf zone. *Coast. Engng* **114**, 177–193.

CHAPLIN, J.R., RAINEY, R.C.T. & YEMM, R.W. 1997 Ringing of a vertical cylinder in waves. *J. Fluid Mech.* **350**, 119–147.

CHOI, S.-J., LEE, K.-H. & GUDMESTAD, O.T. 2015 The effect of dynamic amplification due to a structure's vibration on breaking wave impact. *Ocean Engng* **96**, 8–20.

DERAKHTI, M., KIRBY, J.T., SHI, F. & MA, G. 2016 Wave breaking in the surf zone and deep-water in a non-hydrostatic RANS model. Part 1: organized wave motions. *Ocean Model.* **107**, 125–138.

DEVOLDER, B., TROCH, P. & RAUWOENS, P. 2018 Performance of a buoyancy-modified k-ω and k-ω SST turbulence model for simulating wave breaking under regular waves using OpenFOAM®. *Coast. Engng* **138**, 49–65.

DUBIEF, Y. & DELCAYRE, F. 2000 On coherent-vortex identification in turbulence. *J. Turbul.* **1** (1), 011.

FENTON, J.D. 1988 The numerical solution of steady water wave problems. *Comput. Geosci.* **14** (3), 357–368.

FUHRMAN, D.R. & LARSEN, B.E. 2020 A discussion on "numerical computations of resonant sloshing using the modified isoadvector method and the buoyancy-modified turbulence closure model" [Appl. Ocean Res. (2019), 93, article no. 101829, doi:10.1016.j.apor.2019.05.014]. *Appl. Ocean Res.* **99**, 102159.

FUHRMAN, D.R. & LI, Y. 2020 Instability of the realizable k-ε turbulence model beneath surface waves. *Phys. Fluids* **32**, 115108.

GHADIRIAN, A. & BREDMOSE, H. 2020 Detailed force modelling of the secondary load cycle. *J. Fluid Mech.* **889**, A21.

GRUE, J., BJØRSHOL, G. & STRAND, Ø. 1993 Higher harmonic wave exciting forces on a vertical cylinder. In *Applied Mathematics*, vol. September, pp. 1–30. Matematisk Institutt, Universitetet i Oslo.

GRUE, J. & HUSEBY, M. 2002 Higher-harmonic wave forces and ringing of vertical cylinders. *Appl. Ocean Res.* **24** (4), 203–214.

HALL, M.A. 1958 *Laboratory Study of Breaking Wave Forces on Piles*. Technical Memorandum, vol. 106. Beach Erosion Board.

HONDA, T. & MITSUYASU, H. 1974 Experimental study of breaking wave force on a vertical circular cylinder. *Coast. Engng J.* **17** (1), 59–70.

HSU, T.J., SAKAKIYAMA, T. & LIU, P.L.-F. 2002 A numerical model for wave motions and turbulence flows in front of a composite breakwater. *Coast. Engng* **46** (1), 25–50.

IRSCHIK, K., SPARBOOM, U. & OUMERACI, H. 2004 Breaking wave loads on a slender pile in shallow water. In *29th International Conference of Coast. Eng.* (ed. J. McKee Smith), pp. 568–580. World Scientific.

JACOBSEN, N.G., FUHRMAN, D.R. & FREDSØE, J. 2012 A wave generation toolbox for the open-source CFD library: OpenFOAM®. *Intl J. Numer. Meth. Fluids* **70** (9), 1073–1088.

JANG, H.K., OZDEMIR, C.E., LIANG, J.-H. & TYAGI, M. 2021 Oscillatory flow around a vertical wall-mounted cylinder: flow pattern details. *Phys. Fluids* **33** (2), 025114.

JOSE, J., CHOI, S.-J., GILJARHUS, K.E.T. & GUDMESTAD, O.T. 2017 A comparison of numerical simulations of breaking wave forces on a monopile structure using two different numerical models based on finite difference and finite volume methods. *Ocean Engng* **137**, 78–88.

KAMATH, A., CHELLA, M.A., BIHS, H. & ARNTSEN, Ø.A. 2016 Breaking wave interaction with a vertical cylinder and the effect of breaker location. *Ocean Engng* **128**, 105–115.

KRISTIANSEN, T. & FALTINSEN, O.M. 2017 Higher harmonic wave loads on a vertical cylinder in finite water depth. *J. Fluid Mech.* **833**, 773–805.

KYTE, A. & TØRUM, A. 1996 Wave forces on vertical cylinders upon shoals. *Coast. Engng* **27** (3–4), 263–286.

LARSEN, B.E. & FUHRMAN, D.R. 2018 On the over-production of turbulence beneath surface waves in Reynolds-averaged Navier–Stokes models. *J. Fluid Mech.* **853**, 419–460.

LARSEN, B.E., FUHRMAN, D.R. & ROENBY, J. 2019 Performance of interFoam on the simulation of progressive waves. *Coast. Engng J.* **61** (3), 380–400.

LAUNDER, B.E., REECE, G.J. & RODI, W. 1975 Progress in the development of a Reynolds-stress turbulence closure. *J. Fluid Mech.* **68** (3), 537–566.

LI, Y. & FUHRMAN, D.R. 2021 Computational fluid dynamics simulation of deep-water wave instabilities involving wave breaking. *J. Offshore Mech. Arctic Engng* **144** (2), 021901.

LI, Y., LARSEN, B.E. & FUHRMAN, D.R. 2022 Reynolds stress turbulence modelling of surf zone breaking waves. *J. Fluid Mech.* **937**, A7.

LI, Y., ONG, M.C., FUHRMAN, D.R. & LARSEN, B.E. 2020 Numerical investigation of wave-plus-current induced scour beneath two submarine pipelines in tandem. *Coast. Engng* **156**, 103619.

LIN, P. & LIU, P.L.-F. 1998 A numerical study of breaking waves in the surf zone. *J. Fluid Mech.* **359**, 239–264.

LIU, S., JOSE, J., ONG, M.C. & GUDMESTAD, O.T. 2019 Characteristics of higher-harmonic breaking wave forces and secondary load cycles on a single vertical circular cylinder at different Froude numbers. *Mar. Struct.* **64**, 54–77.

MENTER, F.R. 1994 Two-equation eddy-viscosity turbulence models for engineering applications. *AIAA J.* **32** (8), 1598–1605.

MORISON, J.R., JOHNSON, J.W. & SCHAAF, S.A. 1950 The force exerted by surface waves on piles. *J. Petrol. Tech.* **2** (05), 149–154.

NAOT, D. & RODI, W. 1982 Calculation of secondary currents in channel flow. *ASCE J. Hydraul. Engng* **108** (8), 948–968.

PAULSEN, B.T., BREDMOSE, H., BINGHAM, H.B. & JACOBSEN, N.G. 2014 Forcing of a bottom-mounted circular cylinder by steep regular water waves at finite depth. *J. Fluid Mech.* **755**, 1–34.

QU, S., LIU, S. & ONG, M.C. 2021 An evaluation of different RANS turbulence models for simulating breaking waves past a vertical cylinder. *Ocean Engng* **234**, 109195.

SHIH, T.-H., LIOU, W.W., SHABBIR, A., YANG, Z. & ZHU, J. 1995 A new k-ε eddy viscosity model for high Reynolds number turbulent flows. *Comput. Fluids* **24** (3), 227–238.

SMAGORINSKY, J. 1963 General circulation experiments with the primitive equations: I. The basic experiment. *Mon. Weath. Rev.* **91** (3), 99–164.

SUMER, B.M. & FUHRMAN, D.R. 2020 *Turbulence in Coastal and Civil Engineering*. World Scientific.

WIEGEL, R.L. 1982 Forces induced by breakers on piles. In *18th International Conference on Coast. Eng.* (ed. B. L. Edge), pp. 1699–1715. American Society of Civil Engineers.

WIENKE, J. & OUMERACI, H. 2005 Breaking wave impact force on a vertical and inclined slender pile-theoretical and large-scale model investigations. *Coast. Engng* **52** (5), 435–462.

WILCOX, D.C. 2006 *Turbulence Modeling for CFD*, 3rd edn. DCW Industries.

WILCOX, D.C. 2008 Formulation of the k-ω turbulence model revisited. *AIAA J.* **46** (11), 2823–2838.

XU, F. & WANG, Y. 2021 Numerical simulation of ringing responses of a vertical cylinder. *Ocean Engng* **226**, 108815.